Hindawi
Advances in Materials Science and Engineering
Volume 2024, Article ID 4083427, 13 pages
https://doi.org/10.1155/2024/4083427

Research Article

Mathematical Modeling and Finite Element Analysis of Residual Stress (RS) Field after Multipass Ultrasonic Surface Rolling

Jinggan Shao,[1] **Zhanshu He**,[2] **Genshang Wu**,[1] **Zhi Zhang**,[3] **and Chao Li**[3]

[1]*Henan Key Engineering Laboratory of Building Structure Reinforcement Materials, Henan Jiaoyuan Engineering Technology Group Co., Ltd, Zhengzhou 450005, China*
[2]*Henan Key Engineering Laboratory for Anti-Fatigue Manufacturing Technology, Zhengzhou University, Zhengzhou 450001, China*
[3]*Jinan Sanyue Testing Instrument Co., Ltd, Jinan 250000, China*

Correspondence should be addressed to Jinggan Shao; jysjg@hncc.edu.cn

Received 15 September 2023; Revised 17 January 2024; Accepted 9 February 2024; Published 16 February 2024

Academic Editor: Ivan Giorgio

In order to achieve the change rule of the induced residual stress (RS) field after multipass ultrasonic surface rolling (USR), a mathematical model of the induced residual stress (RS) field after multipass ultrasonic surface rolling is first established. Then, the coupling mechanisms of the RS field after dual-pass USR and multipass USR are analyzed, respectively. Subsequently, a finite element (FE) model is established, and the influence of the interval between two adjacent rolling paths L_S is investigated. Finally, both the mathematical model and the FE model are experimentally verified. The results show that both the mathematical model and the FE model can predict the RS field after multipass USR. Two adjacent RS fields will couple with each other in their overlapping regions. For a relatively small interval L_S, the RS field after multipass USR can be fully coupled, so as to form a uniform compressive RS layer. In this study, when $L_S = 0.05$ mm, the values of the surface compressive RS, the maximum compressive RS, the depth of the maximum compressive RS, and the depth of the compressive RS layer reach 426.71 MPa, 676.54 MPa, 0.05 mm, and 0.54 mm, respectively.

1. Introduction

As a recently developed surface strengthening technology, ultrasonic surface rolling (USR) applies both static force and ultrasonic vibration on the target surface, so as to form a compressive RS layer for extending the fatigue life of the target [1]. Nowadays, USR has attracted extensive attention and has been widely used in aviation, aerospace, automobile, and other fields [2–4]. Jiao et al. [5] established a mathematical model to predict the RS after USR. The results showed that the mathematical model had a high prediction accuracy. Zhang et al. [6, 7] also established a mathematical model to predict the RS after USR. Compared to experimental results, the mathematical model had only an error of 15%. Wang et al. [8] established an FE model of strengthening Ti-6Al-4V by USR. The results showed that the simulation results were in good agreement with the experimental results. Li et al. [9] used ABAQUS/Explicit to establish an FE model of USR. The results showed that the compressive RS increased first and then decreased with the increase of the static force, which agreed well with the experimental results. Khan et al. [10] also used ABAQUS/Explicit to establish an FE model of strengthening AISI304 by USR. The results showed that a larger contact force and a smaller ball could induce a higher compressive RS field. Liu et al. [11] established an FE model of strengthening 40Cr by USR. The results showed that the maximum compressive RS and the depth of the compressive RS layer increased with the static force and the ultrasonic amplitude. Zhu et al. [12] and Gujba et al. [13] strengthened Ti-6Al-4V by USR. They found that the maximum compressive RS could reach 950 MPa and the surface compressive RS could reach 863 MPa.

Although the above references have studied USR by using the mathematical model or FE model, few references have studied it by using both the mathematical model and the FE model. Moreover, much attention is paid to parameter optimization, and little attention is paid to the stress coupling mechanism during multipass USR. Therefore, first, a mathematical model of the induced residual stress (RS) after multipass ultrasonic surface rolling (USR) is established. Then, the coupling mechanisms of the RS field after dual-pass USR and multipass USR are analyzed, respectively. Subsequently, an FE model is established, and the influence of the interval between two adjacent rolling paths L_S is investigated. Finally, both the mathematical model and the FE model are experimentally verified.

2. Mathematical Model

During USR, the ball first extrudes the target surface due to the static force F, as shown in Figure 1(a). Then, it vibrates periodically at a selected frequency f and a selected amplitude A and moves forward at a selected speed v, as shown in Figures 1(b) and (c). In each vibration period, the ball will impact the target once and then move forward at a fixed interval L_P between two adjacent impact locations [13], which is expressed as

$$L_P = \frac{v}{f}. \tag{1}$$

Assuming that the ball is an ideal elastomer, the target is an ideal semi-infinite elastomer, and their contact region is a perfect circle. The contact relationship between the ball and the target is shown in Figure 2, where the dotted lines and the solid lines represent the profiles before and after the two bodies come into contact, respectively. R_1 and R_2 are the initial radii of the ball and the target, respectively, and the radius of the contact surface in the contact region is a_e. δ_1 and δ_2 are the displacements of the centers of the ball and the target, respectively, δ_e is the sum of the normal displacements of the ball and target. So

$$\delta_e = \delta_1 + \delta_2. \tag{2}$$

Supposing a random point along the contact line (red point in Figure 2), its distance from the contact center is r, its normal displacements of the red contact point on the ball and the target are $u_{z1}(r)$ and $u_{z2}(r)$, respectively, and $h_1(r)$ and $h_2(r)$ are the corresponding gaps of the contact point on the ball and the target, respectively. It can be calculated from the geometric relationship:

$$\left.\begin{aligned} h_1(r) &= \frac{r^2}{2R_1}, \\ h_2(r) &= \frac{r^2}{2R_2}. \end{aligned}\right\} \tag{3}$$

So

$$\left.\begin{aligned} u_{z1}(r) &= \delta_1 - h_1(r) = \delta_1 - \frac{r^2}{2R_1}, \\ u_{z2}(r) &= \delta_2 - h_2(r) = \delta_2 - \frac{r^2}{2R_2}. \end{aligned}\right\} \tag{4}$$

It can be concluded from equations (2) and (4):

$$\begin{aligned} u_{z1}(r) + u_{z2}(r) &= \left(\delta_1 - \frac{r^2}{2R_1}\right) + \left(\delta_2 - \frac{r^2}{2R_2}\right), \\ &= \delta_e - \frac{r^2}{2}\left(\frac{1}{R_1} + \frac{1}{R_2}\right). \end{aligned} \tag{5}$$

The schematic diagram of the elastic deformation of the ball after contacting with the target is shown in Figure 3. According to Johnson's Hertz theory [14], the pressure distribution of the two elastomers in contact is expressed as

$$P(r) = P_0\left[1 - \left(\frac{r}{ae}\right)^2\right]^{1/2}. \tag{6}$$

Along the contact line, the distance from the contact center is r and the pressure is $P(r)$. When $r = 0$ (green point in Figures 2 and 3), the pressure reaches the maximum value P_0. The impact force can be derived as follows:

$$F_0 = \int_0^{a_e} P(r) 2\pi r dr = \frac{2\pi a_e^2 P_0}{3}, \tag{7}$$

and the maximum value P_0 can be derived as follows:

$$P_0 = \frac{3F_0}{2\pi a_e^2}. \tag{8}$$

Under the pressure, the normal displacements of points on the ball and the target in the Z direction are as follows [15]:

$$u_{z1}(r) = \frac{1-\mu_T^2}{E_T}\frac{\pi P_0}{4ae}\left(2a_e^2 - r^2\right), \tag{9}$$

$$u_{z2}(r) = \frac{1-\mu_S^2}{E_S}\frac{\pi P_0}{4a_e}\left(2a_e^2 - r^2\right), \tag{10}$$

where E_S and μ_S are Young's modulus and Poisson's ratio of the shot material, respectively, and E_T and μ_T are the Young's modulus and Poisson's ratio of the target material.

It can be concluded from equations (5), (9), and (10):

$$\left(\frac{1-\mu_T^2}{E_T} + \frac{1-\mu_s^2}{E_S}\right)\frac{\pi P_0}{4ae}\left(2ae^2 - r^2\right) = \delta_e - \frac{r^2}{2}\left(\frac{1}{R_1} + \frac{1}{R_2}\right). \tag{11}$$

When $r = 0$ s (green point in Figures 2 and 3), the normal displacement at the center point of the ball is

$$\delta_e = \left(\frac{1-\mu_T^2}{E_T} + \frac{1-\mu_S^2}{E_S}\right)\frac{\pi ae P_0}{2}. \tag{12}$$

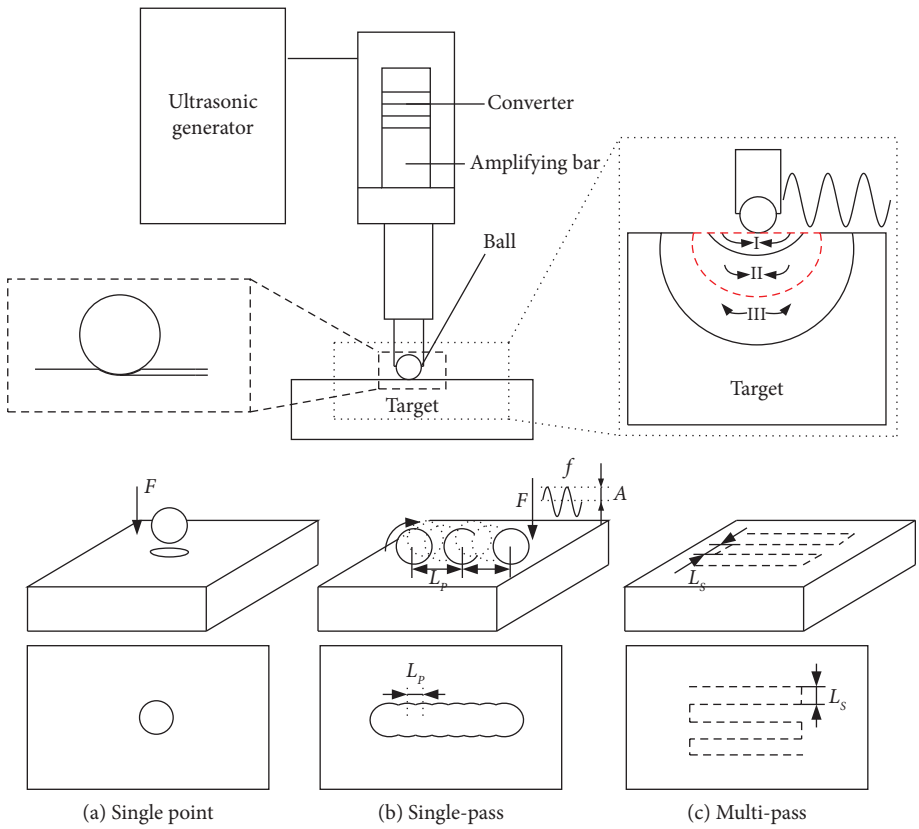

Figure 1: Schematic diagram of USR.

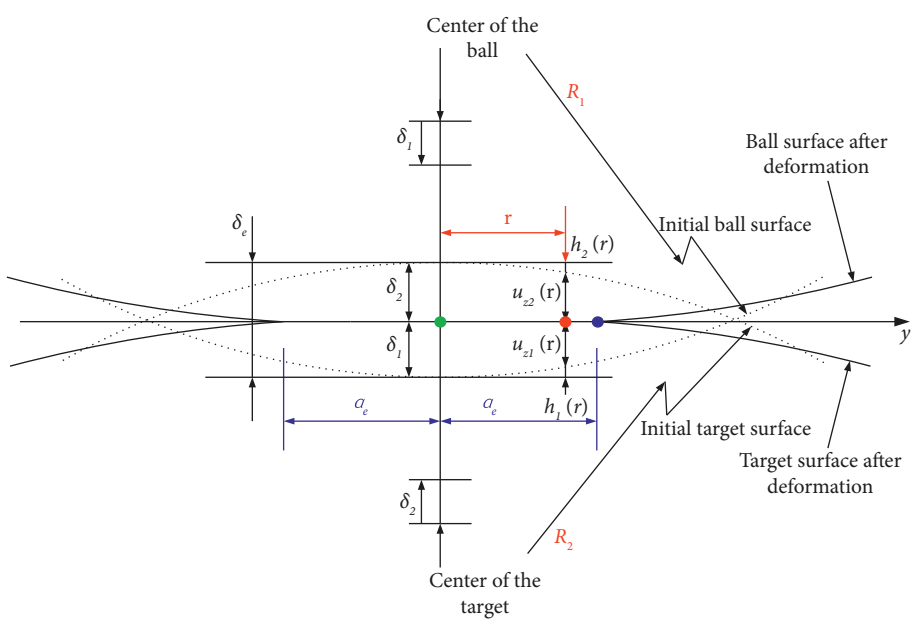

Figure 2: Schematic diagram of contact relationship between the ball and the target.

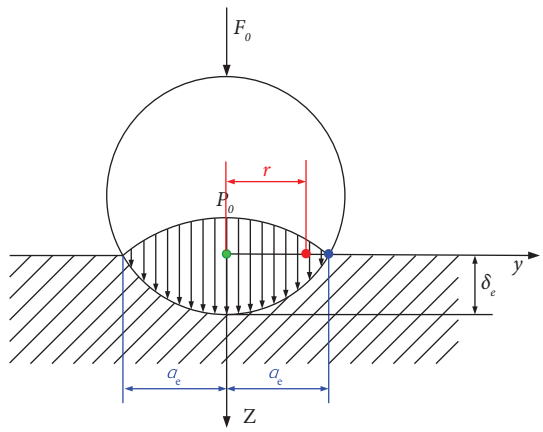

Figure 3: Schematic diagram of elastic deformation after the ball impacts the target.

When $r = a_e$ (blue point in Figures 2 and 3), the contact radius of the ball and the target is

$$a_e = \left(\frac{1-\mu_T^2}{E_T} + \frac{1-\mu_S^2}{E_S}\right)\frac{R_1R_2}{R_1+R_2}\frac{\pi P_0}{2}. \tag{13}$$

It can be concluded from equations (8), (12), and (13):

$$\begin{aligned} a_e &= \sqrt[3]{\frac{3}{4}\frac{R_1R_2}{R_1+R_2}\left(\frac{1-\mu_T^2}{E_T} + \frac{1-\mu_S^2}{E_S}\right)F_0}, \\ \delta &= \sqrt[3]{\frac{9}{16}\frac{R_1R_2}{R_1+R_2}\left(\frac{1-\mu_T^2}{E_T} + \frac{1-\mu_S^2}{E_S}\right)F_0}, \\ P_0 &= \sqrt[3]{\frac{6}{\pi^3}\left(\frac{R_1R_2}{R_1+R_2}\right)^2\frac{F_0}{\left(1-\mu_T^2/E_T + 1-\mu_S^2/E_S\right)^2}}. \end{aligned} \tag{14}$$

In the stage of elastic loading, the stress component of the target material along the depth below the impact point is

$$\begin{aligned} \sigma_x^e(z) = \sigma_y^e(z) &= -P_0\left[(1+\mu_T) - \frac{1}{2}\frac{1}{1+(z/a_e)^2}\right. \\ &\quad \left. -(1+\mu_T)\frac{z}{a_e}\tan^{-1}\left(\frac{z}{a_e}\right)\right], \\ \sigma_z^e(z) &= -\frac{P_0}{1+(z/a_e)^2}, \end{aligned} \tag{15}$$

where z is the depth from the surface.

The equivalent stress and the equivalent strain are

$$\begin{aligned} \sigma_i^e &= \frac{1}{\sqrt{2}}\left[\left(\sigma_x^e - \sigma_y^e\right)^2 + \left(\sigma_y^e - \sigma_z^e\right)^2 + \left(\sigma_z^e - \sigma_x^e\right)^2\right]^{1/2}, \\ \varepsilon_i^e &= \frac{\sigma_i^e}{E_T}. \end{aligned} \tag{16}$$

In fact, the target is elastic-plastic material (i.e., the elastic-plastic strain is induced after the ball impacts the target, as shown in Figure 4. In the stage of elastic loading, the elastic strain is equal to the plastic strain. While in the stage of plastic loading, Li used the following formula to calculate the plastic strain [16]:

$$\varepsilon_i^p = \begin{cases} \varepsilon_i^e, & \varepsilon_i^e < \varepsilon_s, \\ \varepsilon_s + \alpha\left(\varepsilon_i^e - \varepsilon_s\right), & \varepsilon_i^e \geq \varepsilon_s, \end{cases} \tag{17}$$

where α is the ratio of the ideal plastic pit radius to the elastic pit radius and $\alpha = a_p/a_e$. a_p can be solved according to the average pressure between the ball and the target:

$$\int_0^{\delta_p} F_0 d\delta_p = \int_0^{\delta_p} \overline{P} S d\delta_p, \tag{18}$$

where $\overline{P}$ is the average pressure and S is the contact area. It can be obtained from the geometric relationship after the ball impacts the target:

$$R_1^2 = \left(R_1 - \delta_p\right)^2 + a_p^2. \tag{19}$$

R_1 is much bigger than δ_p, so δ_p^2 can be ignored; the contact area S is

$$S = 2\pi R_1 \delta_p. \tag{20}$$

Then, it can be calculated as follows:

$$\begin{aligned} \delta_p &= \frac{F_0}{3\pi R_1 \sigma_S}, \\ a_P &= \left(\frac{2F_0}{3\pi\sigma_S}\right)^{1/2}. \end{aligned} \tag{21}$$

According to the elastic-plastic stress-strain curve shown in Figure 5, the stress equation of the target of elastic-plastic material under different states can be obtained:

$$\sigma_i^p = \begin{cases} \sigma_i^e, & \varepsilon_i^p < \varepsilon_s, \\ \sigma_s + H^1\left(\varepsilon_i^p - \varepsilon_s\right), & \varepsilon_s \leq \varepsilon_i^p < \varepsilon_b, \\ \sigma_b, & \varepsilon_i^p \geq \varepsilon_b, \end{cases} \tag{22}$$

where H^1 is a linear strain-hardening parameter, ε_i^p is the plastic strain, σ_s is yield stress of the target material, σ_b is the ultimate tensile stress of the target material, ε_s is the yield

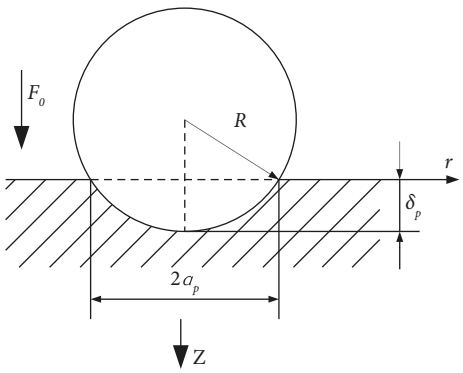

Figure 4: Schematic diagram of elastic-plastic deformation after the ball impacts the target.

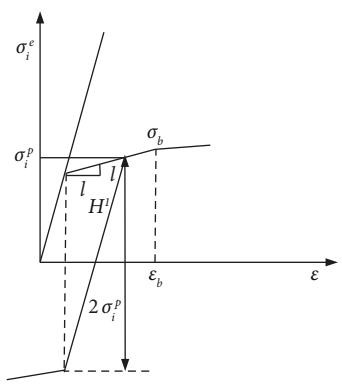

Figure 5: Schematic diagram of elastic-plastic stress-strain.

strain corresponding to the yield stress σ_s, and ε_b is the yield strain corresponding to the yield stress σ_b.

We consider the stage of unloading as an elastic deformation process.

When $\sigma_i^e < \sigma_S$, the transresidual stress is

$$\sigma_i^r = 0. \tag{23}$$

When $\sigma_S \leq \sigma_i^e < 2\sigma_i^p$, the transresidual stress in x, y, z directions is

$$\begin{aligned} \sigma_x^r &= \sigma_y^r = \frac{1}{3}\left(\sigma_i^p - \sigma_i^e\right), \\ \sigma_z^r &= -2\sigma_x^r. \end{aligned} \tag{24}$$

When $2\sigma_i^p \leq \sigma_i^e$, the transresidual stress in x, y, z directions is

$$\begin{aligned} \sigma_x^r &= \sigma_y^r = \frac{1}{3}\left(\sigma_i^p - 2\sigma_i^p - \Delta\sigma_i^p\right), \\ \sigma_z^r &= -2\sigma_x^r, \end{aligned} \tag{25}$$

where $\Delta\sigma_i^p = H^1\Delta\varepsilon_i^p$.

The above calculations can figure out the value of the RS under a single impact. After multipass USR, it is assumed that the stress is evenly distributed on the surface. According to Hooke's law, the stress release amount can be calculated as

$$\sigma_x^{\text{relax}} = \sigma_y^{\text{relax}} = \frac{\mu_T}{1-\mu_T}\sigma_z^r. \tag{26}$$

The induced average RS in x, y, z directions σ_x^R, σ_y^R, and σ_z^R can be calculated according to [17]:

$$\begin{aligned} \sigma_x^R &= \sigma_y^R = \sigma_x^r - \sigma_x^{\text{relax}}, \\ \sigma_z^R &= 0. \end{aligned} \tag{27}$$

By the way, this mathematical model cannot predict the tensile residual stress but can predict the compressive residual stress, and it is only suitable for the 100% coverage rate.

3. Forming and Coupling Mechanism of RS Field

3.1. Forming and Coupling Mechanism of the RS Field after Single-Pass USR. After the ball is applied with both static force and ultrasonic vibration, it will not only roll and move forward continuously but also vibrate and impact the target periodically.

Every time the ball impacts the target, the compressive deformation is formed on the impact region, as the red dotted line shown in Figure 1. When the induced internal stress is larger than the target yield strength, a compressive plastic deformation region (I) is formed. Due to the hindering of the plastic deformation region (I), the compressive elastic deformation region (II) cannot recover completely. For equilibrium, a tensile elastic deformation region (III) will be formed around the compressive elastic deformation region [18]. Finally, a hemispherical RS field with internal compressive stress and external tensile stress is formed, as shown in Figure 6(a).

After the ball vibrates for a single period, a hemispherical RS field is formed. After the ball vibrates for a dual period, the second RS field will be formed and overlap with the first one, as shown in Figure 6(b). In the compressive-compressive overlap region, the compressive RS field is enhanced and becomes larger; in the tensile-tensile overlap region, the tensile RS field is also enhanced and becomes larger. While in the compressive-tensile overlap region, the RS field is weakened and becomes smaller due to the contrary RS.

After the ball rolls along the surface and vibrates for multiperiods, single-pass USR is performed, so that a rolling indentation and an elastic-plastic strain are formed. The RS field induced by each period couples with several adjacent RS fields. As a result, a uniform and continuous RS field is formed in the rolling direction, as shown in Figure 6(c), and a bowl-shaped compressive RS region P and a crescent-shaped tensile RS region Q are formed perpendicular to the rolling direction, as shown in Figure 6(d).

3.2. Coupling Mechanism of the RS Field after Dual-Pass USR. After single-pass USR is finished, the ball hops to the left side with the interval L_S and then continues to roll along the surface, dual-pass USR is performed, and the second

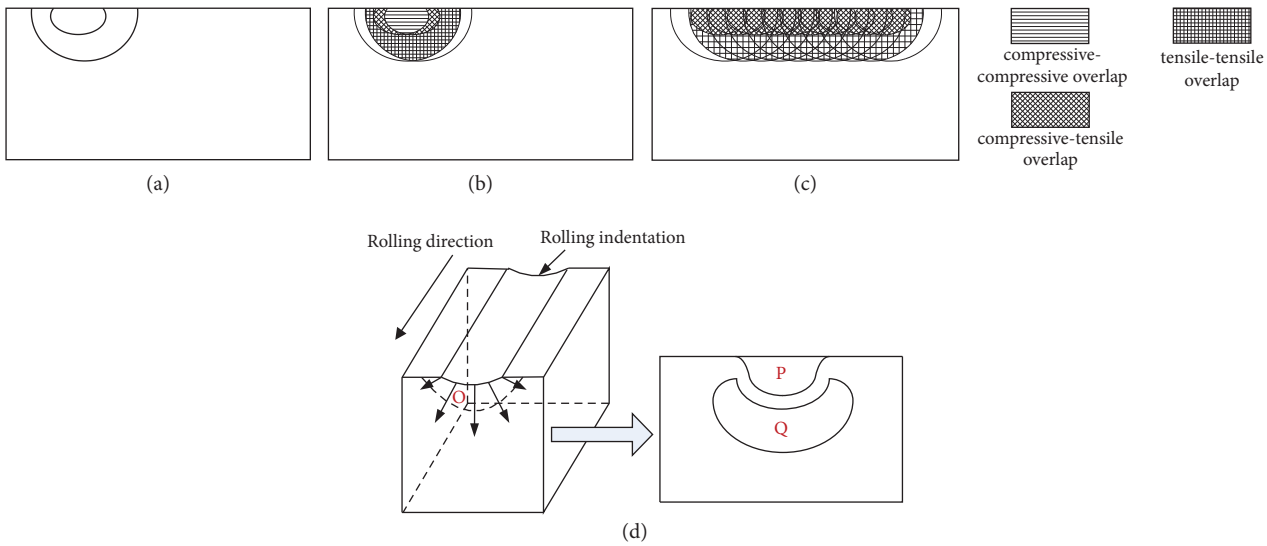

Figure 6: RS field in the rolling direction and perpendicular to the rolling direction after single-pass USR.

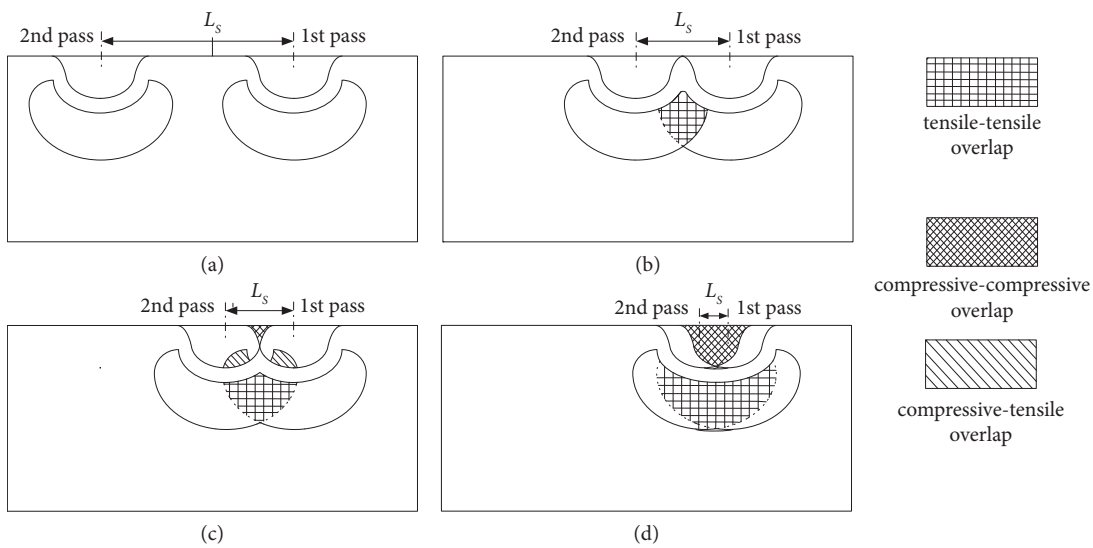

Figure 7: Schematic diagram of the RS field after dual-pass USR.

RS region will be induced. For a relatively large L_S, it is too far for the two RS regions to contact, so the two RS regions will not affect each other, as shown in Figure 7(a). As L_S reduces to a certain value, the two crescent-shaped tensile RS regions begin to overlap with each other, so that the tensile RS field will be enhanced and become larger than that after the first-pass USR, as shown in Figure 7(b). As L_S continues to reduce, the two bowl-shaped compressive RS regions also begin to overlap with each other, so that the compressive RS field will also be enhanced and become larger than that after the first-pass USR, as shown in Figure 7(c). Meanwhile, some bowl-shaped compressive RS regions will also overlap with some crescent-shaped tensile RS regions, so that the RS field will be weakened in these regions due to the contrary RS. As L_S reduces further, both the enhanced tensile RS regions and the enhanced compressive RS regions become larger, while the weakened regions become smaller, as shown in Figure 7(d).

3.3. Coupling Mechanism of the RS Field after Multipass USR. When the ball continues to hop and then rolls multiple times, multipass USR is performed. Then, several adjacent RS regions will appear and overlap with each other, so as to enhance or weaken each other. For achieving a continuous compressive RS layer on the surface, a small L_S is selected. In this condition, several bowl-shaped compressive RS regions overlap together, so as to enhance the compressive RS field and produce a large area compressive RS layer on the surface, as shown in Figure 8. While several crescent-shaped tensile RS regions also overlap together, so as to form a large area tensile RS layer below the surface.

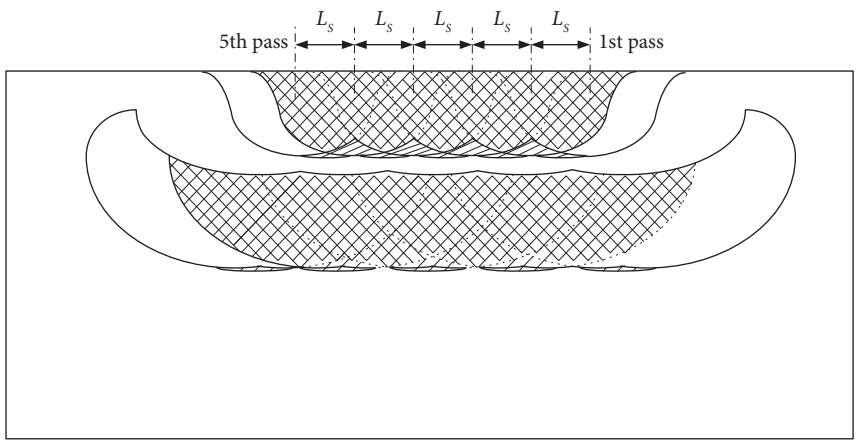

Figure 8: Schematic diagram of the RS field after multipass USR.

Table 1: Mechanical parameters of the target and the ball.

Materials	Target untreated 18CrNiMo7-6	Ball WC alloy
Density ρ_s (kg·m^{-3})	7900	15000
Young's modulus E (GPa)	195	710
Poisson's ratio μ	0.35	0.21
Yield strength σ_s (MPa)	502	—
Yield strain ε_s	0.38%	—
Tensile strength σ_b (MPa)	754	—
Hardening parameter H^1 (MPa)	3177	—

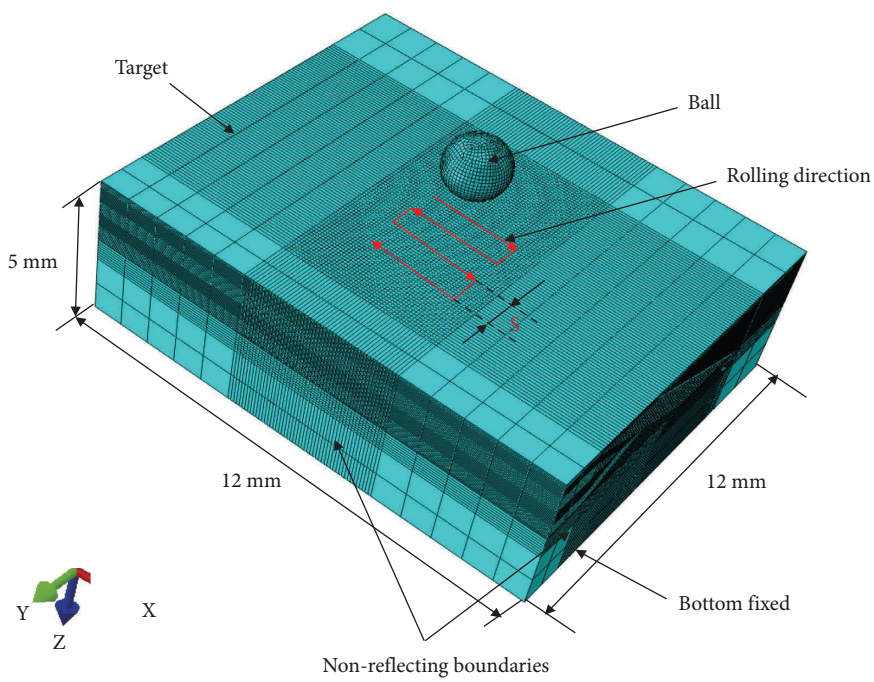

Figure 9: Finite element model of multipass USR.

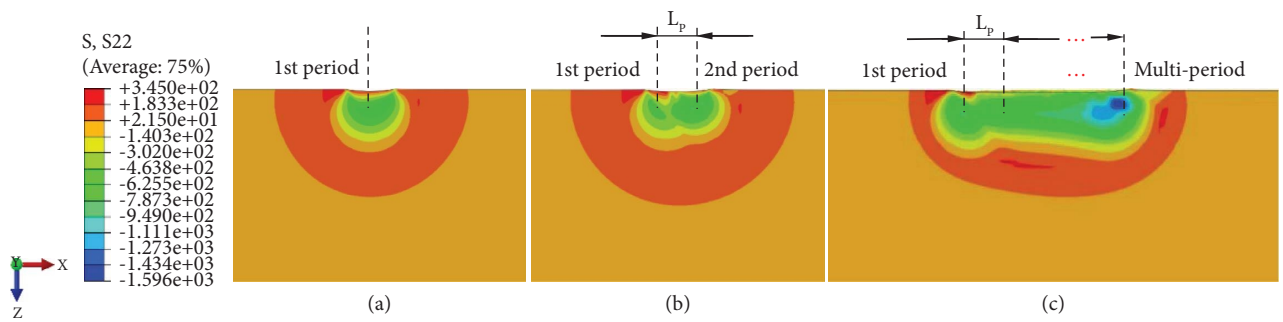

Figure 10: RS field along the depth after single-pass USR: (a) single period, (b) dual period, and (c) multiperiod.

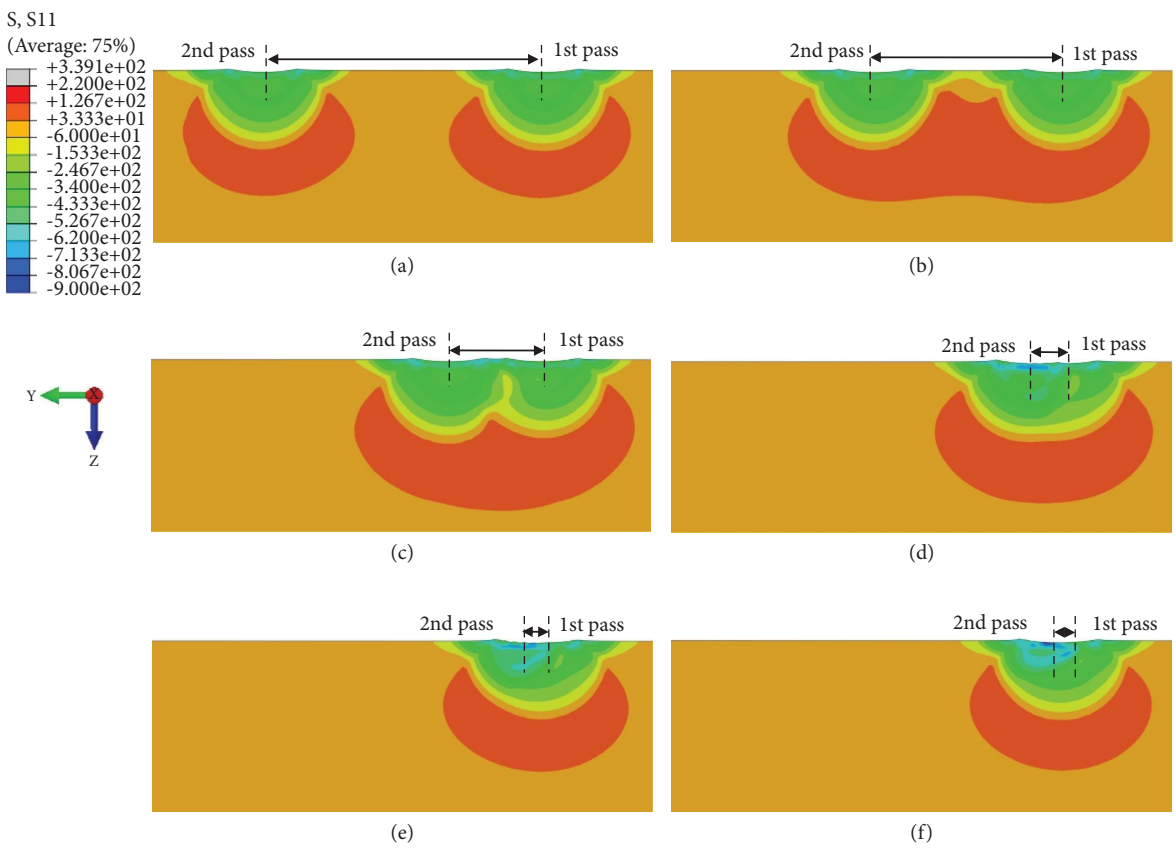

Figure 11: RS field along the depth after dual-pass USR. (a) $L_s = 3$ mm. (b) $L_s = 2$ mm. (c) $L_s = 1$ mm. (d) $L_s = 0.3$ mm. (e) $L_s = 0.1$ mm. (f) $L_s = 0.05$ mm.

4. FE Model

4.1. Material Model. The FE model of multipass USR is established by using ABAQUS/Explicit (version 6.14). For simplifying calculation, some assumptions are made as follows [19]:

(1) The target material is isotropic elastic-plastic

(2) The erosion and the heat after collision between the ball and the target are neglected

(3) The ball is considered rigid as its Young's modulus is much larger than that of the target [10]

As shown in Table 1, an untreated 18CrNiMo7-6 steel is selected as the target material, whose behavior can be approximated by an isotropic bilinear elastic-plastic hardening model.

4.2. Mesh and Boundary Conditions. A target model with a dimension of 12 mm × 12 mm × 5 mm is established (Figure 9). An eight-node linear brick element (C3D8R) with reduced integration and hourglass control is selected to mesh the target, and a bilinear rigid quadrilateral element (R3D4) is selected to mesh the ball. The

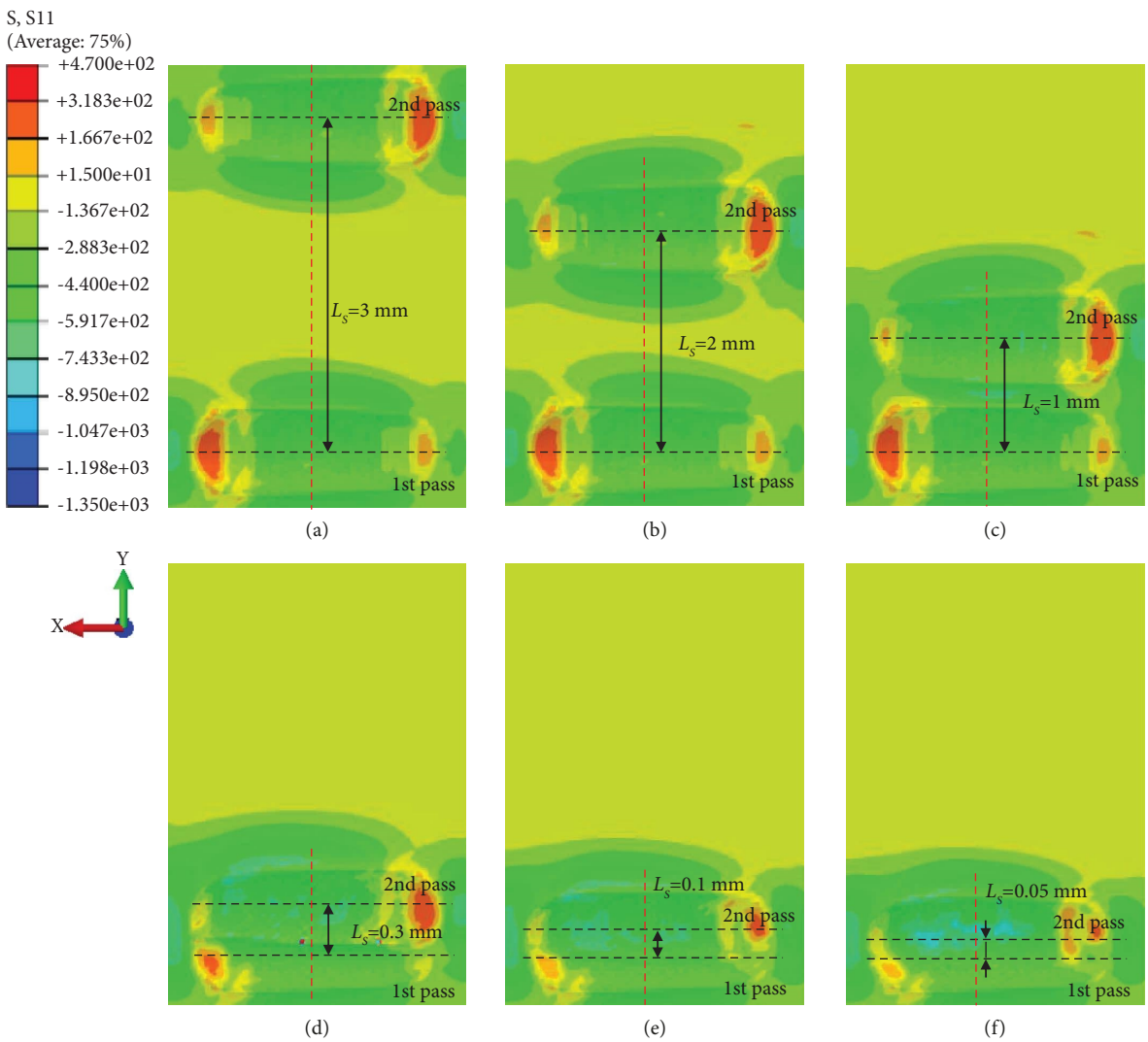

Figure 12: RS field along the surface after dual-pass USR. (a) $L_s = 3$ mm. (b) $L_s = 2$ mm. (c) $L_s = 1$ mm. (d) $L_s = 0.3$ mm. (e) $L_s = 0.1$ mm. (f) $L_s = 0.05$ mm.

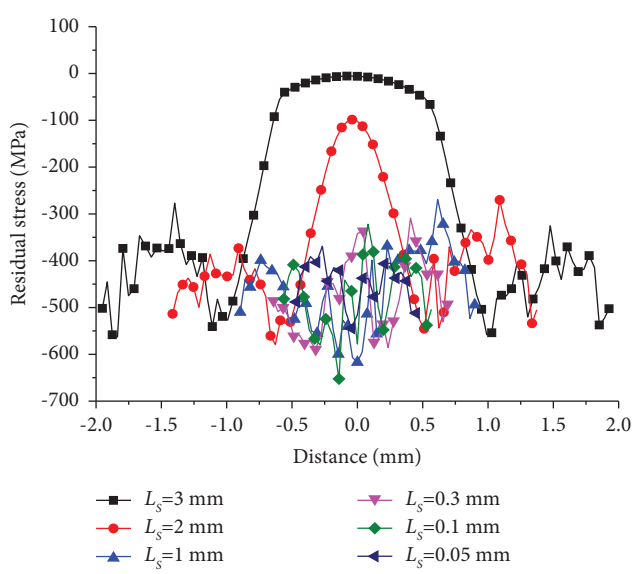

Figure 13: Surface RS curve along the red lines in Figure 12.

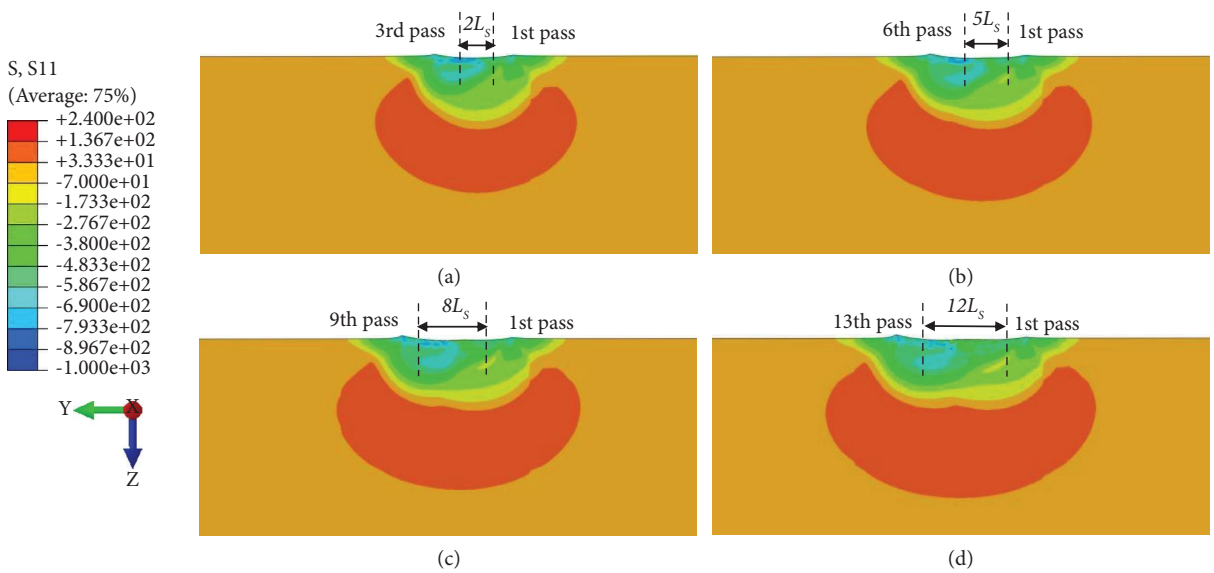

Figure 14: RS field after multipass USR. (a) 3 passes. (b) 6 passes. (c) 9 passes. (d) 13 passes.

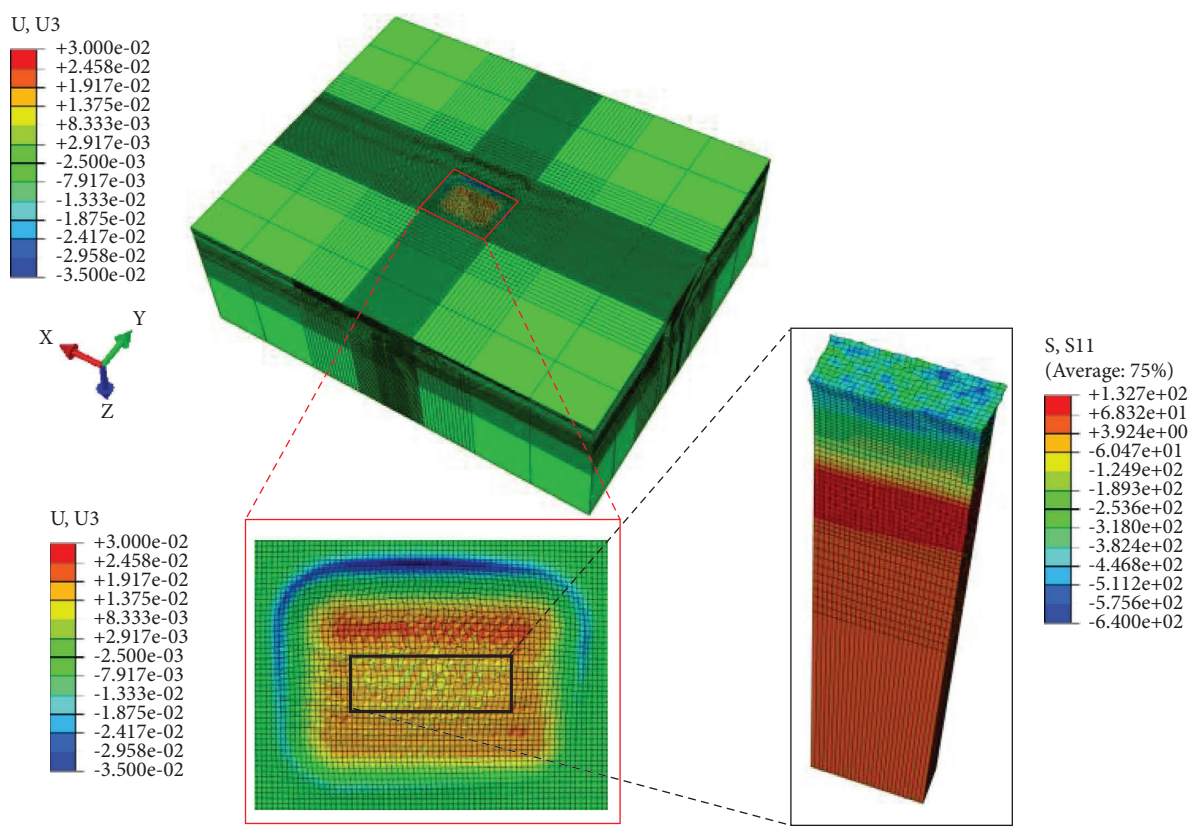

Figure 15: Distribution of the RS field after multipass USR.

load-acting region of the target model is meshed by 0.02 mm elements, its adjacent region is meshed by 0.05 mm elements, and the rest is meshed by 0.5 mm elements. Furthermore, all nodes on the bottom surface are completely fixed, and all four sides are specified as nonreflecting boundaries to eliminate the reflection of stress waves [20].

4.3. Load or Force Applying Information. According to our previous research [21, 22], the parameters of single-pass USR are set as follows: the ball radius $R_1 = 2$ mm, the frequency $f = 30$ kHz, the amplitude $A = 6\ \mu$m, the static force $F = 200$ N, and the interval between two adjacent impact locations $L_P = 0.1$ mm. While the interval L_S between two adjacent rolling paths will be adjusted in the range of 0.05–3 mm.

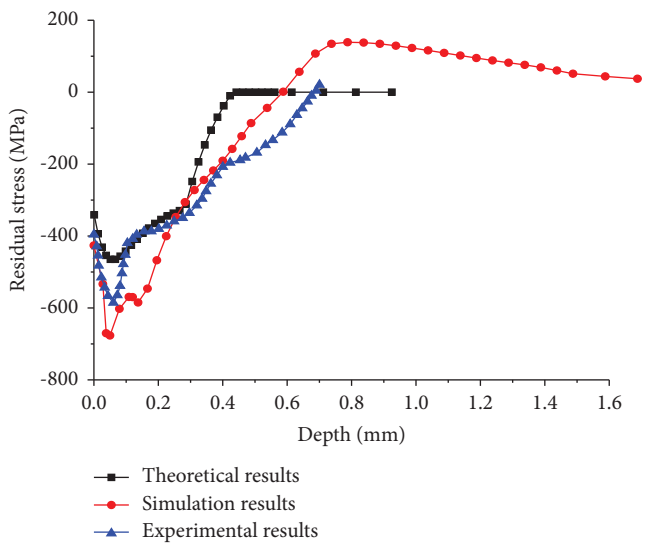

Figure 16: Three RS curves along the depth.

5. Results and Discussion

5.1. Transient Process of RS Field during Single-Pass USR. When the ball vibrates for a single period, it will impact the target downward. After the ball leaves, a small hemispherical RS field forms under the dimple (Figure 10(a)). After the ball rolls and moves $L_P = 0.1$ mm forward, it will vibrate and impact the target for a dual period, the second RS field will couple with the first one, and then the area of the coupled RS field increases (Figure 10(b)). After the ball rolls and moves a few distance, it will vibrate and impact the target for multiperiods (i.e., a single-pass USR), and a uniform and continuous RS field is formed. Along the depth, the compressive RS first increases, then decreases, and finally turns into small tensile RS (Figure 10(c)).

5.2. Influence of L_S on the RS Field after Dual-Pass USR. Next, the influence of the interval L_S on the RS field after dual-pass USR is investigated, as shown in Figure 11. When $L_S = 3$ mm (Figure 11(a)), it is too far for the two RS regions to overlap and affect each other, so a region without any strengthening exists between the two RS regions, which is consistent with the description in Figure 7(a). When L_S reaches 2 mm (Figure 11(b)), the two tensile RS regions begin to overlap and become a large area tensile RS region, which is consistent with the description in Figure 7(b). When L_S reaches 1 mm (Figure 11(c)), the two compressive RS regions also begin to overlap and become a large area compressive RS region. Meanwhile, the tensile RS region becomes small, which is consistent with the description in Figure 7(c). When L_S reaches 0.3 mm (Figure 11(d)), fully coupling of the two RS regions leads to a uniform distributed RS field, and enhancement of the two compressive RS regions results in a larger compressive RS value. When L_S reaches 0.1 mm and 0.05 mm (Figures 11(e) and 11(f)), a more uniform distributed RS field is achieved, which is consistent with the description in Figure 7(d).

Figure 12 shows the surface RS field after dual-pass USR, in which the RS values along the red lines are noted down, as shown in Figure 13. When $L_S = 3$ mm, the two surface compressive RS regions do not overlap, and a zero surface RS region exists between two surface compressive RS regions. When L_S reaches 2 mm, the two compressive surface RS regions begin to overlap, the surface RS between the two surface compressive RS regions is no longer zero but is still close to zero, so the whole surface RS field is uneven. When L_S reaches 1 mm and 0.3 mm, the two surface compressive RS regions overlap and couple with each other, so that a large area surface compressive RS field is formed. While the whole surface RS field is still uneven, a large fluctuation and a clear overlapping line exist. When L_S gradually reaches 0.1 mm and 0.05 mm, the two RS regions become more fully coupled and the RS field becomes more uniform, although the surface compressive RS fluctuates above and below 500 MPa. Especially, when $L_S = 0.05$ mm, the fluctuation is the smallest, and no clear overlapping lines exist, which is favorable to a small surface roughness. Thus, $L_S = 0.05$ mm is considered to be optimal and is selected for studying multipass USR.

5.3. Distribution of the RS Field after Multipass USR. Similarly, several adjacent RS regions after multipass USR will couple with each other, as shown in Figure 14. After multipass USR, the RS field becomes continuous and uniform, leading to a large area compressive RS layer on the surface. Furthermore, the area of the compressive RS layer increases with the increase of the number of USR passes.

The displacement and the internal stress after 15 passes USR are shown in Figure 15. The region between the first pass USR and the last pass USR is highlighted with the red block, and a selection region of the RS field is stood out with the black block. After 15 passes USR, a uniform compressive RS layer is formed. Meanwhile, the surface displacement is uniform; i.e., the surface roughness is still small.

5.4. Comparison of the RS Curve Obtained by the Mathematical Model, FE Model, and Experiment. Under $F = 200$ N, the two RS curves along the depth are calculated by the mathematical model and the FE model and then compared with the experimental RS curve in our previous works [23], as shown in Figure 16. It can be seen that the three RS curves along the depth have the same trend; i.e., the RS first increases from the surface compressive RS to the maximum compressive RS rapidly and then decreases gradually to zero. Furthermore, the three RS curves have close values of the surface compressive RS and the depth of the maximum compressive RS. Therefore, both the mathematical model and the FE model can accurately predict the RS field after multipass USR. In this study, the surface compressive RS, the maximum compressive RS, the depth of the maximum compressive RS, and the depth of the compressive RS layer are 426.71 MPa, 676.54 MPa, 0.05 mm, and 0.54 mm, respectively.

6. Conclusions

(1) Both the mathematical model and the FE model can predict the induced residual stress (RS) field after multipass USR and can be used to optimize ultrasonic surface rolling. Furthermore, these two methods can also be used for studying conventional surface rolling, extrusion, shot peening, and sandblasting.

(2) The adjacent RS fields will couple with each other in their overlapping regions after multipass USR. For a relatively small L_S, the RS field after multipass USR can couple fully, so that a large area uniform compressive RS layer is formed.

(3) When $L_S = 0.05$ mm, the values of the surface compressive RS, the maximum compressive RS, the depth of the maximum compressive RS, and the depth of the compressive RS layer reach 426.71 MPa, 676.54 MPa, 0.05 mm, and 0.54 mm, respectively.

Notations

RS:	Residual stress
USR:	Ultrasonic surface rolling
FE:	Finite element
A:	Amplitude
a_e:	Elastic contact radius
a_p:	Plastic contact radius
E_S, E_T:	Young's modulus of the shot material and the target material
F:	Static force
F_0:	Impact force
f:	Frequency
H^1:	Linear strain-hardening parameter
$h_1(r)$, $h_2(r)$:	Gap of the contact point on the ball and the target
L_P:	Interval between two adjacent impact locations
L_S:	Interval between two adjacent rolling paths
$P(r)$:	Pressure distribution at the contact point
P_0:	Maximum pressure
$\overline{P}$:	Average pressure
R_1, R_2:	Initial radius of the ball and the target
r:	Distance between the contact center and contact point
μ_S, μ_T:	Poisson's ratio of the shot material and the target material
$u_{z1}(r)$, $u_{z2}(r)$:	Normal displacements of the contact point on the ball and the target
v:	Speed
S:	Contact area
z:	Depth from the surface
α:	a_p/a_e
δ_1, δ_2:	Elastic displacement of the centers of the ball and the target
δ_e:	Total elastic displacements of the centers of the ball and target
δ_p:	Total plastic displacements of the centers of the ball and target
σ_b:	Ultimate tensile stress of the target material
σ_s:	Yield stress of the target material
σ_i^e:	Von Mises equivalent elastic stress
σ_x^e, σ_y^e, σ_z^e:	Principal stress in x, y, z directions
σ_i^p:	Plastic stress
σ_i^R:	Induced residual stress
σ_x^R, σ_y^R, σ_z^R:	Induced residual stress in x, y, z directions
σ_x^{relax}, σ_y^{relax}, σ_x^{relax}:	Stress release amount in x, y, z directions
σ_i^r:	Transresidual stress
σ_x^r, σ_y^r, σ_z^r:	Transresidual stress in x, y, z directions
ε_b:	Yield strain corresponding to yield stress σ_b
ε_s:	Yield strain corresponding to yield stress σ_s
ε_i^e:	Von Mises equivalent elastic strain
ε_i^p:	Plastic strain.

Data Availability

The data used to support this study are available from the corresponding author upon request.

Conflicts of Interest

The authors declare that they have no conflicts of interest.

Authors' Contributions

The authors contributed equally to this work.

Acknowledgments

This research was funded by the Henan Provincial Department of Science and Technology (grant number 221111220600), Henan Provincial Department of Transportation (grant number 2019J2), and Henan College of Transportation (grant number 2018JK-05).

References

[1] J. Dang, Q. An, G. Lian et al., "Surface modification and its effect on the tensile and fatigue properties of 300M steel subjected to ultrasonic surface rolling process," *Surface and Coatings Technology*, vol. 422, Article ID 127566, 2021.

[2] J. Dang, H. Zhang, Q. An et al., "Surface integrity and wear behavior of 300M steel subjected to ultrasonic surface rolling process," *Surface and Coatings Technology*, vol. 421, Article ID 127380, 2021.

[3] D. Wang, J. Dang, Y. Li, Z. Liu, H. Wang, and M. Chen, "Study on the surface integrity distribution of 300M ultrahigh strength steel subjected to different surface modification treatments," *Surface and Coatings Technology*, vol. 451, Article ID 129033, 2022.

[4] Z. Peng, X. Zhang, Y. Zhang et al., "Wear resistance enhancement of Inconel 718 via high-speed ultrasonic vibration cutting and associated surface integrity evaluation under high-pressure coolant supply," *Wear*, vol. 530-531, Article ID 205027, 2023.

[5] F. Jiao, S. L. Lan, B. Zhao, and Y. Wang, "Theoretical calculation and experiment of the surface residual stress in the plane ultrasonic rolling," *Journal of Manufacturing Processes*, vol. 50, pp. 573–580, 2020.

[6] M. Zhang, Z. H. Liu, J. Deng, M. J. Yang, Q. L. Dai, and T. Z. Zhang, "Optimum design of compressive residual stress field caused by ultrasonic surface rolling with a mathematical model," *Applied Mathematical Modelling*, vol. 76, pp. 800–831, 2019.

[7] M. Zhang, J. Deng, Z. Liu, and Y. Zhou, "Investigation into contributions of static and dynamic loads to compressive residual stress fields caused by ultrasonic surface rolling," *International Journal of Mechanical Sciences*, vol. 163, Article ID 105144, 2019.

[8] F. Wang, X. H. Men, Y. J. Liu, and X. L. Fu, "Experiment and simulation study on influence of ultrasonic rolling parameters on residual stress of Ti-6Al-4V alloy," *Simulation Modelling Practice and Theory*, vol. 104, Article ID 102121, 2020.

[9] F. Q. Li, B. Zhao, S. L. Lan, and Z. B. Feng, "Experiment and simulation of the effect of ultrasonic rolling on the surface properties of Ti-6Al-4V," *The International Journal of Advanced Manufacturing Technology*, vol. 106, no. 5-6, pp. 1893–1900, 2020.

[10] M. K. Khan, M. E. Fitzpatrick, Q. Y. Wang, Y. S. Pyoun, and A. Amanov, "Effect of ultrasonic nanocrystal surface modification on residual stress and fatigue cracking in engineering alloys," *Fatigue and Fracture of Engineering Materials and Structures*, vol. 41, no. 4, pp. 844–855, 2018.

[11] Y. Liu, X. Zhao, and D. Wang, "Effective FE model to predict surface layer characteristics of ultrasonic surface rolling with experimental validation," *Materials Science and Technology*, vol. 30, no. 6, pp. 627–636, 2014.

[12] Y. L. Zhu, K. Wang, L. Li, and Y. L. Huang, "Evaluation of an ultrasound-aided deep rolling process for anti-fatigue applications," *Journal of Materials Engineering and Performance*, vol. 18, no. 8, pp. 1036–1040, 2009.

[13] A. K. Gujba, Z. C. Ren, Y. L. Dong, C. Ye, and M. Medraj, "Effect of ultrasonic nanocrystalline surface modification on the water droplet erosion performance of Ti-6Al-4V," *Surface and Coatings Technology*, vol. 307, pp. 157–170, 2016.

[14] K. L. Johnson, *Contact Mechanics*, Cambridge University Press, New York, NY, USA, 1985.

[15] M. Zhang, Z. He, Y. Zhang et al., "Theoretical and finite element analysis of residual stress field for different geometrical features after abrasive waterjet peening," *Journal of Pressure Vessel Technology*, vol. 141, no. 1, 2018.

[16] J. K. Li, Y. Mei, W. Duo, and W. Renzhi, "Mechanical approach to the residual stress field induced by shot peening," *Materials Science and Engineering*, vol. 147, no. 2, pp. 167–173, 1991.

[17] H. Y. Miao, S. Larose, C. Perron, and M. Lévesque, "An analytical approach to relate shot peening parameters to Almen intensity," *Surface and Coatings Technology*, vol. 205, no. 7, pp. 2055–2066, 2010.

[18] Z. S. He, S. S. Zhao, T. Fu et al., "Experimental and numerical analysis of water jet peening on 6061 aluminum alloy," *Journal of Pressure Vessel Technology*, vol. 140, no. 2, 2018.

[19] Z. S. He, C. Li, S. S. Zhao et al., "Mathematical model and verification of residual stress induced by water jet peening," *Metals*, vol. 9, p. 936, 2019.

[20] Z. S. He, B. B. Cui, S. S. Zhao et al., "Numerical simulation of surface topography and residual stress after abrasive water jet sequential peening," *Proceedings of the Institution of Mechanical Engineers, Part L: Journal of Materials: Design and Applications*, vol. 235, no. 4, pp. 777–795, 2021.

[21] Z. S. He, J. L. Yu, B. B. Cui et al., "Finite element analysis of residual stress induced by single-pass ultrasonic surface rolling process," *Transactions of the Indian Institute of Metals*, vol. 75, no. 5, pp. 1113–1123, 2022.

[22] Z. S. He, H. X. Yu, S. S. Zhao et al., "An experimental and numerical analysis of water jet peening of Al6061-T6," *The International Journal of Advanced Manufacturing Technology*, vol. 107, no. 9-10, pp. 3833–3845, 2020.

[23] Z. H. Liu, T. Z. Zhang, M. J. Yang, Q. L. Dai, and Y. X. Zhang, "Performance analysis of surface modification layer of 18CrNiMo7-6 gear steel treated by ultrasonic rolling," *Journal of Zhengzhou University*, vol. 41, pp. 44–49, 2020.